Inhibition of PIKfyve kinase prevents infection by EBOV and SARS-CoV-2

Yuan-Lin Kang[1,2,3], Yi-Ying Chou[1,2,4], Paul W. Rothlauf[5,6], Zhuoming Liu[5], Timothy K. Soh[6], David Cureton[6,7], James Brett Case[8], Rita E. Chen[5,8], Michael S. Diamond[5,8], Sean P. J. Whelan[5,*], Tom Kirchhausen[1,2,9,*]

[1]Department of Cell Biology, Harvard Medical School, 200 Longwood Av, Boston, MA 02115, USA
[2]Program in Cellular and Molecular Medicine, Boston Children's Hospital, 200 Longwood Av, Boston, MA 02115, USA
[3]Present Address: Department of Stem Cell and Regenerative Biology, Harvard University, 7 Divinity Ave, Cambridge, MA 02138, USA
[4]Present Address: Biogen, 225 Binney Street, Cambridge, MA 02142, USA
[5]Department of Molecular Microbiology, Washington University in Saint Louis, 660 South Euclid Avenue, Saint Louis, MI 63110, USA
[6]Program in Virology, Harvard Medical School, 200 Longwood Ave, Boston, MA 02115, USA
[7]Boehringer Ingelheim Animal Health, Inc. 3239 Satellite Blvd Duluth, GA 30096, USA
[8]Departments of Medicine and Pathology & Immunology, Washington University in Saint Louis, 660 South Euclid Avenue, Saint Louis, MI 63110, USA
[9]Department of Pediatrics, Harvard Medical School, 200 Longwood Av, Boston, MA 02115, USA

[*] Corresponding authors:
Dr. Tom Kirchhausen
Harvard Medical School
kirchhausen@crystal.harvard.edu
phone: 617.713.8888 / fax: 617.713.8898

Dr. Sean Whelan
spjwhelan@wustl.edu
Washington University in Saint Louis
phone: 314.286.1585

37 ***Running title:*** **Drug inhibitors of EBOV and SARS-CoV-2 virus infection**

38

39 ***Keywords:*** **COVID-19, EBOV, SARS-CoV-2, inhibition, Apilimod, Vacuolin-1,**
40 **PIKfyve, pandemic**

Virus entry is a multistep process. It initiates when the virus attaches to the host cell and ends when the viral contents reach the cytosol. Genetically unrelated viruses can subvert analogous subcellular mechanisms and use similar trafficking pathways for successful entry. Antiviral strategies targeting early steps of infection are therefore appealing, particularly when the probability for successful interference through a common step is highest. We describe here potent inhibitory effects on content release and infection by chimeric VSV containing the envelope proteins of EBOV (VSV-EBOV) or SARS-CoV-2 (VSV-SARS-CoV-2) elicited by Apilimod and Vacuolin-1, small molecule inhibitors of the main endosomal Phosphatidylinositol-3-Phosphate/Phosphatidylinositol 5-Kinase, PIKfyve. We also describe potent inhibition of SARS-CoV-2 strain 2019-nCoV/USA-WA1/2020 by Apilimod. These results define new tools for studying the intracellular trafficking of pathogens elicited by inhibition of PIKfyve kinase and suggest the potential for targeting this kinase in developing a small-molecule antiviral against SARS-CoV-2.

INTRODUCTION

Membrane-enveloped viruses deliver their contents to cells via envelope protein-catalyzed membrane fusion. Binding of virus to specific host cell receptor(s) triggers membrane fusion, which can occur directly at the plasma membrane or following endocytic uptake. Viruses that require endocytic uptake can use different initial trafficking routes to reach the site of membrane fusion. In endosomes, acidic pH serves to triggers conformational rearrangements in the viral envelope proteins that catalyze membrane fusion, as seen for influenza A virus (IAV) and vesicular stomatitis virus (VSV). For Ebola virus (EBOV), proteolytic processing of the envelope protein by host cell proteases (1) is necessary to expose the receptor binding domain prior to engagement of Neiman Pick C1 (NPC1 or NPC Intracellular Cholesterol Transporter 1) – the late endosomal-lysosomal receptor protein (2). Proteolytic processing is also required for severe acute respiratory syndrome coronavirus (SARS-CoV) (3, 4), and for the current pandemic SARS-CoV-2 (5). Lassa fever virus (LASV) uses a different mechanism, binding alpha-dystroglycan at the plasma membrane (6), for internalization with a subsequent pH-regulated switch that leads to engagement of lysosomal associated membrane protein 1 (LAMP1) for membrane fusion (7). Lymphocytic choriomeningitis virus (LCMV) also uses alpha-dystroglycan (6) and is internalized in a manner that depends on endosomal sorting complexes required for transport (ESCRT) proteins (8), although it remains unknown whether a second receptor is required.

A hallmark of the endolysosomal system is controlled dynamic trafficking of vesicular carriers among its various sub-compartments. Phophoinositides are markers for defining the identity of these sub-compartments because they are restricted in their distribution to specific intracellular membranes [reviewed in (9)]. Although it is one of the least abundant of the phosphoinositides in cells, PI(3,5)P2 is particularly important for endomembrane homeostasis. It is produced by PIKfyve, which phosphorylates the D-5 position in phosphatidylinositol-3-phosphate (PI3P) to yield phosphatidylinositol 3,5-bisphosphate (PI(3,5)P2) (10). First cloned as mammalian p235 (11), PIKfyve is a 240 kDa class III lipid kinase, present on the cytosolic face of endosomal membranes (12, 13) as part of a ternary complex with SAC and ArPIKfyve (14).

Ablation of PIKfyve function by genetic (12, 15) or pharmacological means (16-20) causes endosomal swelling and vacuolation of late endosomes and endolysosomes. It is thought that these changes result from decreased membrane fission and concomitant interference in endosomal traffic (13, 21). Small-molecule inhibitors of PIKfyve, all of

92 which have some structural resemblance to each other, have been studied as potential
93 drugs for treating cancer and autoimmune diseases. These inhibitors include Apilimod
94 (19), Vacuolin-1 (18), a series of 30 Vacuolin-related molecules (22), YM201636 (16),
95 and WX8 chemical family members (20). Physiological effects of these compound in
96 cells include inhibition of autophagy (17, 22, 23), reduced generation of IL-12/IL-23 (24),
97 and reduced dendritic cell infiltration in psoriasis (25).
98
99 Apilimod also inhibits infection by several viruses, including ZEBOV. Although it does
100 not alter the pH of endosomes nor inhibit cathepsin B or L (26), Apilimod blocks entry of
101 ZEBOV and other pathogenic filoviruses (27). Several groups reported that Apilimod
102 prevents colocalization of VSV-ZEBOV pseudoviruses with the EBOV endosomal
103 receptor NPC1, but does not prevent colocalization with early endosomal antigen 1
104 (EEA1) (5, 27, 28). Apilimod also inhibits entry of pseudotyped viruses bearing the spike
105 proteins of MERS-CoV, SARS-CoV, and SARS-CoV-2, as well as of authentic mouse
106 hepatitis virus (MHV) particles (5).
107
108 Here, we have studied the effects of Apilimod on infection of VSV-eGFP-SARS-CoV-2
109 and VSV-eGFP-ZEBOV chimeras and showed that Apilimod blocks infection of both,
110 with an IC50 of ~50 nM. Apilimod and Vacuolin-1 also prevented entry and infection of
111 VSV-MeGFP-ZEBOV and many of the internalized VSV-MeGFP-ZEBOV virions
112 colocalized with NCP1 in the distended, vacuolated endosomes. This suggests that
113 blocking PIKfyve kinase has the same downstream effects on these viruses, even
114 though VSV-eGFP-SARS-CoV-2 does not require interaction with NPC1 for membrane
115 fusion. Apilimod also inhibits infection by authentic SARS-CoV-2 strain 2019-
116 nCoV/USA-WA1/2020 virus, with an IC50 slightly lower than its IC50 for the VSV-eGFP-
117 SARS-CoV-2. We suggest that Apilimod, which has passed safety tests in previous
118 human clinical trials for non-viral indications (24, 25, 29, 30), is a potential starting point
119 for developing small-molecule entry inhibitors of SARS-CoV-2 that could limit infection
120 and disease pathogenesis.

121 ## RESULTS

122 **Apilimod inhibits infection of VSV-MeGFP-LCVM and VSV-EBOV.** We inoculated
123 SVG-A cells with vesicular stomatitis virus (VSV) chimeras expressing the viral matrix
124 protein (M) fused to eGFP (MeGFP). The chimeras include VSV (VSV-MeGFP, which
125 initiates fusion at pH<6.2), VSV-V269H G (VSV-MeGFP-V269H, a variant of VSV G that
126 initiates fusion at pH<5.8), rabies virus G (VSV-MeGFP-RABV), Lassa virus GP (VSV-
127 MeGFP-LASV), lymphocytic choriomeningitis virus GP (VSV-MeGFP-LCMV) or Zaire
128 Ebola virus GP (VSV-MeGFP-ZEBOV). Following the incubation protocol summarized
129 in **Fig 1A**, we tested the effects on infection of Apilimod or Vacuolin-1; both compounds
130 are small-molecule inhibitors of PIKfyve kinase, which generates PI(5)P and PI(3,5)P2
131 in late endosomes and lysosomes. Using a flow cytometry based-assay to monitor a
132 single round of infection determined by expression of viral MeGFP (**Fig. 1B**), we found
133 that Apilimod and Vacuolin-1 potently inhibit VSV-MeGFP-ZEBOV infection (**Fig. 1C**).
134 These results agree with results obtained by others with Apilimod (26, 31), in different
135 cell types infected with MLV virus pseudotyped with EBOV G or with Ebola virus itself
136 (26, 27, 32). Apilimod was a less effective inhibitor of VSV-MeGFP-LCMV infection, and
137 Vacuolin-1 had no effect at the concentration used. In contrast, Apilimod and Vacuolin-1
138 failed to prevent infection by VSV-MeGFP, VSV-MeGFP-V269H, VSV-MeGFP-RABV,
139 or VSV-MeGFP-LASV (**Fig. 1C**). IN1 (33), an inhibitor of the phosphoinositide kinase
140 Vps34, the main endosomal generator of PI3P, also interfered with VSV-MeGFP-LCMV
141 and VSV-MEGFP-ZEBOV infection (**Fig. 1C**). All of these viruses require low pH to
142 trigger viral membrane fusion with the endosomal membranes, and as expected,
143 infection was fully blocked by Bafilomycin A1, which inhibits the vacuolar type H^+-
144 ATPase (V-ATPase) acidification activity (**Fig. 1C**).
145

146 **Apilimod and Vacuolin-1 prevent cytoplasmic entry of VSV-MEGFP-ZEBOV.**
147 Productive infection requires delivery of the viral ribonucleoprotein core (RNP) into the
148 cytosol**.** In these experiments, we deemed RNP delivery, as monitored by single cell
149 fluorescence microscopy imaging (experimental protocol summarized in **Fig. 2A** and
150 **3A**), to be successful when fluorescent MeGFP encapsulated in the incoming virus
151 appeared at the nuclear margin of infected cells. The representative examples of VSV
152 infection and RNP core release shown in **Fig. 2B** were obtained in the absence or
153 presence of cycloheximide, which prevents viral protein expression. In the absence of
154 cycloheximide (*left panel*), large amounts of newly synthesized MeGFP are present
155 throughout the cell. In the presence of cycloheximide (*right panel*), we observed MeGFP
156 in virions (fluorescent spots) as well as released MeGFP concentrated at the nuclear

157 margin. We scored the effect of Apilimod, Vacuolin-1 or IN1 on RNP delivery by VSV-
158 MeGFP, VSV-MeGFP-V269H and VSV-MeGFP-ZEBOV by determining the appearance
159 of MeGFP at the nuclear margin in cycloheximide-treated cells. Consistent with the
160 infection results, Apilimod, Vacuolin-1 and IN1 prevented entry of VSV-Me-GFP-EBOV
161 but not of VSV-MeGFP or VSV-MeGFP-V296H. As expected, Bafilomycin A1blocked
162 entry of all viruses (images in **Fig. 2C** and quantification in **Fig. 2D**).
163
164 **Intracellular trafficking of virus particles in the presence of Apilimod or Vacuolin-**
165 **1.** Internalized virus particles traffic along the endocytic pathway to reach the
166 endosomal compartment(s) from which membrane fusion and genome entry into the
167 cytosol occur. To establish the identity of the endosomal compartments, we used
168 genome-editing in SVG-A cells to replace expression of a subset of proteins enriched in
169 different endosomal compartments (the small GTPases Rab5c and Rab7a, EEA1, or
170 NPC1) with their corresponding fluorescent chimeras obtained by fusion with TagRFP,
171 mScarlet, or Halo (**Fig. 3B, 3C, 3E, 3F, 4B-E**). The lack of fluorescently tagged fillipin (a
172 cholesterol binder) in the endolysosomal compartment in the absence but not in the
173 presence of U18666A, a potent inhibitor of NPC1 (**Fig 4F**), showed that NPC1-Halo
174 remained active as a cholesterol transporter.
175
176 Using live-cell spinning disk confocal microscopy, we monitored the presence of virus
177 particles in the fluorescently tagged endosomes by colocalization with the fluorescent
178 spots from the virus-incorporated MeGFP. We monitored entry by carrying out the
179 experiments in the presence of cycloheximide, thus ensuring that any MeGFP
180 fluorescent signal at the nuclear margin originated only from MeGFP molecules carried
181 by incoming viral particles (**Fig. 3C**). All cells were maintained at 37°C throughout all
182 phases of the experiment to ensure normal and undisturbed intracellular trafficking. All
183 control experiments performed in the absence of inhibitors showed arrival of VSV-
184 MeGFP, VSV-MeGFP-V296H, or VSV-MeGFP-ZEBOV virus particles to early (Rab5c
185 and EEA1) (**Fig. 3D, 4E**) or late endosomes and lysosomes (Rab7a or NPC1) (**Fig. 3G,**
186 **4C, 4E**). MeGFP released from all viruses appeared at the nuclear margin, showing
187 effective RNP release. NPC1, the receptor for VSV-MeGFP-ZEBOV entry is required for
188 fusion from endosomes (2). The successful VSV-MeGFP-ZEBOV infection observed in
189 the absence of drug in cells expressing NPC1-Halo alone or in combination with
190 mScarlet-EEA1 indicates that NPC1-Halo is capable of facilitating infection and that
191 VSV-MeGFP-ZEBOV trafficked to NPC1-Halo-containing endosomes.

192 Apilimod and Vacuolin-1 treatment of the SVG-A cells led to enlargement and
193 vacuolization of their endosomes and lysosomes tagged with fluorescent EEA1, Rab5c,
194 Rab7a or NPC1 (**Fig. 3-5**), in agreement with earlier PIKfyve ablation studies (13, 21).
195 VSV-MeGFP and VSV-MeGFP-V296H (fluorescent dots, white) reached all tagged
196 species of enlarged endolysosomes and successfully penetrated into the cytosol, as
197 indicated by MeGFP at the nuclear margin (**Fig. 3E, 3F and 4C, 4D**). VSV-MeGFP-
198 ZEBOV also trafficked to all tagged species of enlarged endolysosomes, often reaching
199 one of the numerous NPC1-containing vacuoles enriched in EEA1 (**Fig. 5C**). VSV-
200 MeGFP-ZEBOV in EEA1-containing endosomes increased in the presence of Apilimod,
201 as also reported for VLP EBOV (27). While able to reach NPC1-containing functional
202 endosomes in cells treated with Apilimod, VSV-MeGFP-ZEBOV failed to penetrate into
203 the cytoplasm, as reflected by absence of MeGFP in the nuclear margin (**Fig. 5B**).
204
205 **Apilimod blocks infection of VSV SARS-CoV-2.** Using a recombinant vesicular
206 stomatitis virus (VSV) expressing soluble eGFP (VSV-eGFP) where the glycoprotein (G)
207 was replaced with that of ZEBOV G (VSV-eGFP-EBOV) or SARS-CoV-2 (VSV-eGFP-
208 SARS-Cov-2). We inoculated MA104 cells with these chimera viruses and tested the
209 effects of Apilimod on infection by flow cytometry (**Fig. 6A**). We found potent inhibition
210 of VSV-eGFP-SARS-CoV-2 infection by Apilimod and confirmed that the compound
211 also inhibits VSV-eGFP-ZEBOV infection (**Fig. 6B, 6C**). The dose-response curves
212 indicated similar effects for VSV-eGFP-ZEBOV and VSV-eGFP-SARS-CoV-2 (IC50s ~
213 50 nM), in contrast to the absence of any detectable inhibition of VSV-eGFP infection,
214 used here as a negative control.
215
216 **Apilimod blocks infection of SARS-CoV-2 virus.**
217 To test the effect of Apilimod on bona fide SARS-CoV-2 infection, we exposed Vero E6
218 cells to fully infectious SARS-CoV-2 (strain 2019-nCoV/USA-WA1/2020); after 24 h
219 incubation, supernatants were harvested and tittered by focus-forming assay on a
220 separate set of Vero E6 cells (**Fig. 7A**). Apilimod strongly inhibited SARS-CoV-2
221 infection, and the dose-response curve was similar or better than those observed for
222 VSV-eGFP-ZEBOV or VSV-eGFP-SARS-CoV-2 (IC50s ~ 10 nM) (**Fig. 7B**).

DISCUSSION

Coronaviruses, filoviruses, and arenaviruses have different replication strategies and unrelated surface glycoproteins that engage different receptor molecules during entry (1, 2, 5-8). Coronavirus and filovirus surface glycoproteins share a requirement for entry associated proteolytic processing for activation as fusogens (1) Filoviruses require passage through low pH compartments where cathepsins are active. Coronaviruses may enter directly by fusion at the plasma membrane or following receptor mediated endocytosis. Cell entry of SARS-CoV and SARS-CoV-2 depends on the protease TMPRSS2 in conjunction with ACE2 (34-37), and when TMPRSS2 is present, the entry pathway becomes insensitive to cathepsin inhibition (34, 37, 38).

The common inhibition of viruses from all three groups by Apilimod is a consequence of perturbing their shared entry pathway. Moreover, it is not the cathepsin activity itself that these compounds affect, judging from the outcome of the assays with Apilimod and Vacuolin-1 showing they inhibit VSV chimeras bearing the surface glycoproteins of ZEBOV and LCMV and to a lesser extent LASV. Apilimod also inhibits infection of cells by VSV-SARS-CoV-2 as well as by authentic SARS-CoV-2; neither compound blocks infection by wild-type VSV. For VSV-ZEBOV, we have shown that the virus reaches a compartment enriched in NPC1, the EBOV co-receptor, and often also enriched in EEA1, but that it nonetheless fails to release internal proteins into the cytosol. Apilimod does not inhibit cathepsin (26) but Apilimod (39) and Vacuolin-1 (17, 23) can interfere with cathepsin maturation as evidenced by an increase in pro-cathepsin in treated cells; they don't influence endosomal pH (18, 26, 40) although other studies report Apilimod decreases cathepsin activity (41) and Vacuolin-1 increases pH (17, 23). Irrespective of this discrepancy, both Apilimod and Vacuolin-1 inhibit PI-3P-5-kinase (PIKfyve) (17, 19), a three-subunit complex (14) with a PI-3P-binding FYVE domain (10, 11) that recognizes the endosomal marker, PI-3-P. Functional ablation of this enzyme by genetic means (12, 15) gives rise to the same cellular phenotype as treatment with either compound (17-19). The similar dose-response curves for Apilimod inhibition of the ZEBOV and SARS-CoV-2 chimeras (IC50 of ~ 50 nM) and of authentic SARS-CoV-2 virus (IC50 ~ 10 nM) are in good agreement with the IC50 of ~ 15 nM for Apilimod inhibition of PIKfyve *in vitro* (19). Thus, perturbing normal endosomal trafficking by inhibiting PIKfyve activity suggests it is the mechanism by which Apilimod and Vacuolin-1 block entry of such a diverse set of viral pathogens.

258 One of the most striking consequence of PIKfyve inhibition, and hence of PI-3,5-P_2
259 restriction in endosomal membranes, is the swelling of endosomes into small, spherical
260 vacuoles - the phenomenon that gave Vacuolin-1 its name (18). Our imaging data with
261 VSV-MeGFP-ZEBOV chimeras show that the virus particles accumulating in these
262 structures, many of which also contain the NPC1 co-receptor (2, 42), often appear to be
263 relatively immobile and adjacent to the endosomal limiting membrane. One possible
264 explanation is that when a virion reaches these distended endosomes, it can bind or
265 remain bound to the limiting membrane, but not fuse. Another is that virions may fuse
266 with smaller intraluminal vesicles in the endosomal lumen (43), but that PI-3,5-P2
267 depletion prevents back fusion of these vesicles with the endosomal limiting membrane
268 and inhibits release into the cytosol of the viral genome.
269
270 Inhibition of infection by authentic SARS-CoV-2 shows that the blocked release of the
271 viral genome from a vacuolated endosome is independent of the shape, size, and
272 distribution of spike protein on the virion. The assay we used to determine effects on
273 infectivity of authentic virus measured release of virions after multiple rounds of
274 infection, rather than entry, which we monitored in the VSV-SARS-CoV-2 experiments
275 by detecting eGFP synthesis in the cytosol. Nevertheless, the IC50 of Apilimod in
276 experiments with authentic virus is remarkably similar (or even better) to that obtained
277 with chimeric VSV-SARS-CoV-2.
278
279 Although cathepsin L inhibitors block SARS-CoV and SARS-CoV-2 infection in cell
280 culture (4, 5), they have less pronounced effects when tested in animals (44). This may
281 because another protease, TMPRSS2 on the surface of cells in relevant tissues,
282 appears to prime SARS-CoV (44) and SARS-CoV-2 (37) spike proteins for efficient
283 entry. As the effectiveness of Apilimod and Vacuolin-1 does not depend on cathepsin
284 inhibition, their capacity to block entry of several distinct families of viruses is likely to be
285 independent of the identity of the protease that primes their surface glycoprotein for
286 fusion. Phase I and phase II clinical trials have shown that Apilimod is safe and well-
287 tolerated (24, 25, 29, 30). The trials were discontinued because of lack of effectiveness
288 against the autoimmune condition for which the drug was tested. We suggest that one
289 of these compounds, or a potential derivative, would be a candidate broad-spectrum
290 therapeutic for several emerging human viral pathogens, including SARS-CoV-2.

291 # FIGURE LEGENDS

292 **Figure 1. Apilimod and Vacuolin-1 inhibit VSV-MeGFP-ZEBOV infection.**

293 **(A)** Schematic of infectivity assay, where SVG-A cells were pretreated for 1 hour with 5
294 μM Vacuolin, 5 μM Apilimod, 5 μM IN1, or 10 nM BAF A1 and subsequently infected
295 with VSV-MeGFP (multiplicity of infection, MOI = 2), VSV-MeGFP-V296H (MOI = 1),
296 VSV-MeGFP-RABV (MO I= 0.6), VSV-MeGFP-LASV (MOI = 0.6), VSV-MeGFP-LCVM
297 (MOI = 0.6) or VSV-MeGFP-ZEBOV (MOI = 0.6) for 1 hour in the presence of drugs.
298 The cells were then washed to remove unbound virus and incubated for the indicated
299 times in the presence of drugs. The cells were then fixed and the percentage of cells
300 expressing viral MeGFP was measured by flow cytometry.

301 **(B)** Representative flow cytometry results of an infection assay using VSV-MeGFP-
302 EBOV.

303 **(C)** Quantification of the infectivity is shown with averages from three independent
304 experiments per condition each determined as a duplicate measurement (error bars
305 show SEM). The statistical significance was determined using a one-way ANOVA and
306 Tukey *post-hoc* test (*, $P \leq 0.05$; **, $P \leq 0.01$; ***, $P \leq 0.001$).

307

308 **Figure 2. Apilimod and Vacuolin-1 inhibit VSV-MeGFP-ZEBOV.**

309 **(A)** Schematic of entry assay where SVG-A cells were infected with VSV-MeGFP (MOI
310 = 4), VSV-MeGFP-V296H (MOI = 4), or VSV-MeGFP-ZEBOV (MOI = 4). Experiments
311 were performed in the presence of 5 ug/mL cycloheximide (CHX) to prevent protein
312 synthesis. Entry assay was based on the appearance of MeGFP fluorescence on the
313 nuclear margin on a per cell basis, of fixed infected cells visualized by fluorescence
314 microscopy. Staining the fixed cells with Alexa647 labeled wheat germ agglutinin
315 identified the plasma membrane of each cell (dashed outlines in **C**).

316 **(B)** Virus infection in the absence of CHX (left panel) resulted in the appearance of
317 MeGFP fluorescence throughout the cell volume. The presence of CHX resulted in virus
318 entry being observed by MeGFP fluorescence at the nuclear margin, which was
319 released from incoming viral particles (right panel, white arrows). Scale bar indicates 10
320 μm.

321 **(C)** Representative examples of maximum-Z projections images from the whole cell
322 volume obtained with optical sections separated by 0.3 um using spinning disc confocal
323 microscopy. Scale bar indicates 10 μm.

324 **(D)** Quantification of the number of cells with nuclear margin labeling from three
325 independent experiments each determined from fields containing 59-90 cells (error bars

326 show SEM). The statistical significance of the entry data was analyzed for statistical
327 significance by one-way ANOVA and Tukey post-hoc test (***, P ≤ 0.001).
328
329 **Figure 3. Endolysosomal traffic of VSV-MeGFP-ZEBOV in cells expressing**
330 **TagRFP-Rab5c or TagRFP-Rab7a in the presence of Apilimod or Vacuolin-1.**
331 **(Associated Videos 1 and 2).**
332 **(A)** Schematic of live cell imaging experiment using SVG-A cells expressing
333 fluorescently tagged TagRFP-Rab5c or TagRFP-Rab7a. Cells were infected with VSV-
334 MeGFP, VSV-MeGFP-V296H or VSV-MeGFP-ZEBOV (MOI = 4). Viruses trafficking
335 (monitored with MeGFP) to the endo-lysosomal system (recognized by their labeling
336 with TagRFP-Rab5c or TagRFP-Rab7a) and virus entry (established by MeGFP at the
337 nuclear margin) were ascertained by live-cell florescence imaging using a spinning disc
338 confocal microscope.
339 **(B)** Visualization of VSV-MeGFP infection in TagRFP-Rab5c cells in the absence (left
340 panel) or presence of CHX (right panel, white arrows) using live-cell imaging. Scale bar
341 represents 10 µm.
342 **(C)** Genomic PCR analysis of SVG-A cells showing biallelic integration of TagRFP into
343 the *RAB5C* genomic locus by cotransfection of a plasmid coding for Cas9, a linear PCR
344 product coding for the specific gRNAs targeting a region near the ATG codon of Rab5c
345 under the control of the U6 promoter, and a template plasmid containing the RFP
346 sequence flanked by 800 base pairs upstream and downstream of the targeted region
347 (see materials and methods for more details) to generate a clonal gene-edited cell-line
348 expressing TagRFP-Rab5c.
349 **(D)** Representative examples of maximum-Z projection images from four optical
350 sections spaced 0.35 um apart of virus entry in the absence of drug, or in the presence
351 of IN1, Vacuolin, or Apilimod (from left to right) for VSV (top), VSV-V269 (middle), and
352 VSV EBOV (bottom). Each condition is in the presence of CHX. All viruses reach
353 Rab5c-containing endosomes but only VSV-MeGFP-ZEBOV fails to penetrate in the
354 presence of IN1, Vacuolin-1, or Apilimod. Scale bars are 10 µm. Insets correspond to a
355 single optical section with scale bars of 3 µm.
356 **(E)** Visualization of VSV infection in TagRFP-Rab7a cells in the absence of CHX (left
357 panel) and entry in the presence of CHX (right panel, white arrows) with scale bar
358 indicating 10 µm.
359 **(F)** Genomic PCR analysis showing biallelic integration of RFP into the *RAB7A* genomic
360 locus to generate a clonal gene-edited cell-line expressing TagRFP-Rab7a, using the
361 same approach as used for Rab5C.

362 **(G)** Representative examples of maximum-Z projection images of virus entry (in the
363 presence of CHX) in the absence of drug, or in the presence of IN1, Vacuolin, or
364 Apilimod (from left to right) for VSV-MeGFP (top), VSV-MeGFP-V296H (middle), and
365 VSV-MeGFP-ZEBOV (bottom). All viruses reach Rab7a-containing endosomes but
366 only VSV-MeGFP-ZEBOV fails to penetrate in the presence of IN1, Vacuolin-1 or
367 Apilimod. Scale bars are 10 µm. Insets correspond to a single optical section with scale
368 bars of 3 µm.
369
370 **Figure 4. Endolysosomal traffic of VSV-MeGFP-ZEBOV in cells expressing NPC1-**
371 **Halo or coexpressing mScarlet-EEA1 and NPC1-Halo in the presence of Apilimod.**
372 **(Associated Video 3).**
373 **(A)** Schematic of live cell imaging experiment with gene-edited SVG-A cells expressing
374 NPC1-Halo or NPC1-Halo together with mScarlet-EEA1. Halo was labeled with either
375 JF549 or JF647. Cells were infected with VSV-MeGFP-ZEBOV (MOI = 3).
376 **(B)** Genomic PCR analysis showing biallelic integration of Halo into the *NPC1* genomic
377 locus to generate a clonal gene-edited cell-line expressing NPC1-Halo, using the same
378 approach as for Rab5C and Rab7A.
379 **(C)** Representative examples of maximum-Z projection images from four optical
380 sections spaced 0.25 um apart in the absence (left) and presence of Apilimod (right)
381 showing that VSV-MeGFP-ZEBOV reached NPC1-Halo-containing endosomes even in
382 the presence of Apilimod, while failing to penetrate and infect. Scale bar indicates 10
383 µm. Insets correspond to a single optical section with the scale bar indicating 3 µm.
384 **(D**) SVG-A cells with genomic NPC1-Halo were further gene edited to contain EEA1
385 tagged with mScarlet. Genomic PCR analysis shows biallelic integration into the *EEA1*
386 locus of mScarlet-EEA1 (left) and into the *NPC1* locus of NPC1-Halo (right).
387 **(E)** Representative examples of maximum-Z projection images in the absence (left) and
388 presence of Apilimod (right) showing that VSV-MeGFP-ZEBOV reached endosomes
389 containing mScarlet-EEA1 and endosomes containing both mScarlet-EEA1 and NPC1-
390 Halo in the presence of Apilimod, while failing to penetrate and infect. Scale bar
391 indicates 10 µm. Insets correspond to a single optical section with scale bar indicating 3
392 µm.
393 **(F)** Representative images of parental (top) and gene-edited SVG-A cells expressing
394 NPC1-Halo (bottom) incubated with filipin III (naturally fluorescent polyene antibiotic
395 that binds to cholesterol) in the absence (left) and presence of U18666A (right, NPC1
396 inhibitor of cholesterol export) showing NPC1-Halo is a functional cholesterol
397 transporter.

398

399 **Figure 5. Extent of VSV-MeGFP-ZEBOV traffic into endosomes enriched in in**
400 **NPC1-Halo or NPC1-Halo and mScarlet-EEA1.**
401 **(A)** Schematic of imaging experiment of VSV-EBOV trafficking in NPC1-Halo or NPC1-
402 Halo and mScarlet-EEA1 gene edited SVG-A cells.
403 **(B)** Representative examples of maximum-Z projection images from four optical
404 sections spaced 0.25 um apart in the absence and presence of Apilimod after 2 or 4
405 hours post infection.
406 **(C)** Quantification of VSV-MeGFP-EBOV colocalization with mScarlet-EEA1 alone, both
407 mScarlet-EEA1 and NPC1-Halo, or NPC1-Halo alone. At 2 hours post infection, 73 and
408 95 cells were quantified in the absence or presence of 5 μM Apilimod, respectively. At 4
409 hours, 55 and 147 cells were quantified in the absence or presence of 5 μM Apilimod,
410 respectively. Data is presented as % colocalization within the three types of labeled
411 endosomes.
412

413 **Figure 6. Apilimod and Vacuolin-1 inhibit infection of VSV-eGFP-SARS-Cov-2**
414 **(A)** Schematic of infectivity assay of VSV-eGFP, VSV-eGFP-ZEBOV, and VSV-eGFP-
415 SARS-CoV-2 in MA104 cells. MA104 cells were pretreated for 1 h with the indicated
416 concentration Apilimod. Pretreated cells were inoculated with the indicated virus (MOI =
417 1) for 1h at 37°C. At 6 hours post infection cells were harvested and the fraction of cell
418 expressing eGFP cells quantified by flow cytometry.
419 **(B)** Quantification of the infectivity is shown with averages +/- SEM from three
420 independent experiments. Statistical significance was determined using a T-test (*, $P \leq$
421 0.05; **, $P \leq 0.01$).
422

423 **Figure 7. Apilimod inhibits infection of SARS-CoV-2 virus**
424 **(A)** Schematic of infectivity assay of fully infectious Sars-CoV-2 (strain 2019-nCoV/USA-
425 WA1/2020). Vero E6 cell monolayers were pretreated with medium containing DMSO
426 or serial dilutions of Apilimod at the indicated concentrations. SARS-CoV-2 was diluted
427 (MOI = 0.01) in Apilimod-containing medium and added to Vero E6 cells for 1 h at 37°C.
428 After adsorption, the viral inocula were removed, and medium containing the respective
429 concentration of Apilimod was reapplied. After 24 h incubation, supernatants were
430 harvested and tittered by focus-forming assay on a separate set of Vero E6 cells.
431 **(B)** Quantification of the infectivity is shown with averages +/- SEM from three
432 independent experiments per condition and expressed as the percent inhibition relative
433 to mock-treated SARS-CoV-2 infected cells.

434

435 **Video 1. Apilimod doesn't inhibit VSV-MeGFP entry.** Maximal Z-projection from four optical
436 sections separated 0.25 um apart of SVG-A cells gene-edited to express TagRaFP-Rab5c
437 imaged by spinning disc confocal microscopy every 3 seconds for 3 min. Cells were infected
438 with VSV-MeGFP (MOI = 4) in the presence of CHX with or without 5 uM Apilimod and imaged
439 ~ 3-4 hr post-infection.

440

441 **Video 2. Apilimod inhibits VSV-MeGFP-ZEBOV entry.** Maximal Z-projection from four optical
442 sections separated 0.25 um apart of SVG-A cells gene-edited to express TagRFP-Rab5c
443 imaged by spinning disc confocal microscopy every 3 seconds for 3 min. Cells were infected
444 with VSV-MeGFP-ZEBOV (MOI = 3) in the presence of CHX with or without 5 uM Apilimod and
445 imaged ~ 6-7 hr post infection.

446

447 **Video 3. Apilimod inhibits VSV-MeGFP-ZEBOV entry.** Maximal Z-projection from four optical
448 sections separated 0.25 um apart of SVG-A cells gene-edited to express NPC1-Halo imaged by
449 spinning disc confocal microscopy every 3 seconds for 3 min. Cells were infected with VSV-
450 MeGFP-ZEBOV (MOI = 3) with or without 5 uM Apilimod and imaged ~ 5 hr post infection.

451 # MATERIAL AND METHODS

452 **Cell culture**

453 Human astroglial SVG-A derived cells (a kind gift from Walter J. Atwood) were grown at
454 37°C and 5% CO_2 in Minimum Essential Medium (MEM) (10-010-CV; Corning)
455 supplemented with 10% heat inactivated fetal bovine serum (S11150; Atlanta
456 Biologicals), penicillin and streptomycin (1406-05-9; VWR International). African Green
457 Monkey kidney epithelial MA104 cells (a kind gift from Siyuan Ding, WUSM) were grown
458 at 37°C and 5% CO_2 in Medium 199 supplemented with 10% heat inactivated fetal
459 bovine serum. Vero C1008 [Vero 76, clone E6, Vero E6] (ATCC CRL-1586) cells were
460 cultured in Dulbecco's Modified Eagle Medium (DMEM) supplemented with 10% fetal
461 bovine serum, and penicillin and streptomycin. Vero CCL-81 (ATCC CCL-81) cells were
462 maintained in DMEM supplemented with 10% FBS, 10mM HEPES pH 7.4, 1%
463 Glutamax, and penicillin/streptomycin.

464

465 **Reagents**

466 Vacuolin-1 (18) was custom synthesized; Apilimod (HY-14644) was from MedChem
467 Express, IN1 was a kind gift from Dr. N. Gray (33), U-18666A (10009085), and Fillipin III
468 (70440) were from Cayman Chemical, Bafilomycin A1 (B1793-2UG) was from Sigma-
469 Aldrich, Cycloheximide (239764) was from Calbiochem, and wheat germ agglutinin
470 conjugated with Alexa Fluor®-647 (W32466) was from ThermoFisher.

471

472 **Viruses**

473 Recombinant VSV (Indiana serotype) expressing MeGFP alone which initiates fusion at
474 pH<6.2 (VSV-MeGFP) (45) (or in combination with V269H G, VSV-MeGFP-V296H),
475 RABV G (VSV-MeGFP- RABV) (46), LASV G (VSV-MeGFP-LASV) (7), LCMV G (VSV-
476 MeGFP-LCMV), Zaire EBOV G (VSV-MeGFP-ZEBOV) (47) or SARS-CoV-2 S Wuhan-
477 Hu-1 strain (VSV-eGFP-SARS-CoV-2 – description to be published elsewhere) were
478 used for infection, entry and live cell imaging assays. All viruses were generated and
479 recovered according to (48).

480

481 SARS-CoV-2 strain 2019-nCoV/USA-WA1/2020 was obtained from the Centers for
482 Disease Control and Prevention (gift of Natalie Thornburg). Virus was passaged once in
483 Vero CCL81 cells (ATCC) and titrated by focus-forming assay also on Vero E6 cells.

484

485 **Genome-editing**

486 Individual cell lines of SVG-A were gene edited in both alleles using the CRISPR/Cas9
487 system to incorporate fluorescent tags into the N-terminus of Rab5c (TagRFP), Rab7a
488 (TagRFP), EEA1 (mScarlet) or the C-terminus of NPC1 (Halo). The NPC1-Halo
489 expressing cells were further gene edited to incorporate mScarlet-EEA1 creating SVG-A
490 cells simultaneously expressing mScarlet-EEA1 and Halo-NPC1-Halo.
491
492 A free PCR strategy (49, 50) was used to generate small guide RNAs (sgRNA) with
493 target sequences for either Rab5c, Rab7a, NPC1, or EEA1.
494
495 The genomic DNA fragment of Rab5c, Rab7a, NPC1, or EEA1 genes fused with either
496 RFP, Halo, or mScarlet were cloned into the pUC19 vector (donor constructs) which
497 then served as homologous recombination repair templates for the Cas9 enzyme-
498 cleaved genomic DNA. Donor constructs were obtained by a ligation of PCR
499 amplification products from the genomic DNA fragments, TagRFP, Halo, and mScarlet
500 sequences. Primers F1-R1 and F3-R3 amplified approximately 800 base pairs of
501 genomic sequences upstream and downstream of the start codon of Rab5c, Rab7a or
502 EEA1, or the stop codon of NPC1, respectively. Primers F1 and R3 contain sequences
503 complementary to the pUC19 vector linearized using the SmaI restriction enzyme (lower
504 case in the primer sequences). The TagRFP sequence containing the GGS peptide
505 linker was amplified using primers F2-R2 from a TagRFP mammalian expression
506 plasmid used as a template. The F2 primer contains complementary sequences to the
507 3' end of the F1-R1 fragment, while the F3 primer contains complementary sequences
508 to the 3' end of the TagRFP sequences. PCR products (fragments F1-R1, F2-R2, and
509 F3-R3) were subjected to electrophoresis in 1% agarose and gel purified using a
510 purification kit from Zymogen. The PCR fragments were cloned into the linearized
511 pUC19 vector using the Gibson Assembly Cloning Kit (E5510S; New England Biolabs).
512
513 Primer sequences used to generate the sgRNAs and corresponding genomic
514 fragments:

Primer Description		Sequence
U6 promoter	forward primer	5' GCCGGTACCTGAGGGCCTATTTCCC 3'
	reverse primer	5'ACCTCTAGAAAAAAAGCACCGACTCGGTGCCACTTTTTCAAGTTGATAACGGACTAGCCTTATTTTAACTTGCTATTTCTAGCTCTAAAACN NNNNNNNNNNNNNNNNNNCGGTGTTTCGTCCTTTCCACAAG 3
target sequence for reverse primer	rab5c	GACCCGCCATTGCCCGTCCA
	rab7a	TCAAACTAAAGGGGGAAAAG
	NPC1	TAAATTTCTAGCCCTCTCGC
	EEA1	GGTGGTGGTTAAACCATG
Rab5c	F1	gaattcgagctcggtacccGAGAGAACTAGGGAAGAAGGATCAG
	R1	TGCCCGTCCAGCTGTAGTG
	F2	CCACTACAGCTGGACGGGCAatggtgtctaagggcgaagagc
	R2	GGAACCACCAGAACCACCAGAA
	F3	GGTTCTGGTGGTTCTGGTGGTTCCCTGGCGGGTCGGGGAGGCGCA
	R3	gtcgactctagaggatccccCCTCCTACCAAGAGAGTAGAGAAAG
Rab7a	F1	gaattcgagctcggtacccACTGCTGTCAGCCTTGCCTTCA
	R1	CCTTCAAACTAAAGGGGGAAAAGG
	F2	CCTTTTCCCCCTTTAGTTTGAAGGatggtgtctaagggcgaag
	R2	GGAACCACCAGAACCACCAGAA
	F3	TTCTGGTGGTTCTGGTGGTTCCACCTCTAGGAAGAAAGTGTTGCTG
	R3	gtcgactctagaggatccccCCTCACCCAACCTACCACAGAAT
NPC1	F1	gaattcgagctcggtacccCCACTGAGATGAAGGAGTCCAT
	R1	GAAATTTAGAAGCCGTTCGCGC
	F2	CGCGAACGGCTTCTAAATTTCggaggttctggtggttctggtggttccGCAGAAATCGGTACTGGCTTTCCA
	R2	GCCGGAAATCTCGAGCGTCGACAG
	F3	CTGTCGACGCTCGAGATTTCCGGCtagccctctcgcagggcatcc
	R3	gtcgactctagaggatccccGCTGTCTAATGAAACTTCTAGGTC
EEA1	F1	gaattcgagctcggtacccCTCTTTGGCTGAAATTAGAAGCAGG
	R1	CATGGTTTAACCACCACCCGGCG
	F2	CGCCGGGTGGTGGTTAAACCATGgtgagcaagggcgaggcagtgat
	R2	cttgtacagctcgtccatgccgc
	F3	GCGGCATGGACGAGCTGTACAAGggaggttctggtggttctggtggttccTTAAGGAGGATTTTACAGAGGGTAAGAG
	R3	gtcgactctagaggatccccGCTCTAATCTTTCTATCCTCAAGGTTTTC

SVG-A cells (1.5 x 10^5 cells) were co-transfected with 0.8 µg of *Streptococcus pyogenes* Cas9, 0.8 µg free PCR product coding for the target sgRNA, and 0.8 µg pUC19 vector using Lipofectamine 2000 reagent (Invitrogen) according to the manufacturer's instructions. Transfected cells were grown for 7 to 10 days and sorted for TagRFP, Halo, or mScarlet expression using fluorescence-activated cell sorting (FACS) (SH-800S; Sony). Prior to FACS, NPC1-Halo cells were labeled for 15 minutes with Janelia Fluor™ 647 (JF647). Single cells expressing the desired chimera were isolated, clonally expanded, and then screened by genomic PCR for TagRFP, Halo, or mScarlet insertion into both alleles.

Primer sequences used for screening:

Primer	Description	Sequence
Rab5C	typing forward	GAGCCTGAAGTTGGGAGACC
	typing reverse	CATGCCCACTCACCTCCAAT
Rab7a	typing forward	GCGGTCACTTCTTTGAGAAAGT
	typing reverse	AAGTGGCAGCACGGACAGTGT
NPC1	typing forward	TCTCCAAAAGAGAGGGAGAGAGAT
	typing reverse	AAGTTTAGTGTCCTGTGGTTGCCT
EEA1	typing forward	CATCTGTCAGTTACGGGGGCTG
	typing reverse	CGGCACCACACCCTCCAGCTC

528 **Infection assays**

529 SVG-A cells were plated at about 30-40 % confluency into 24-well plates and incubated
530 for 1 day at 37°C and 5% CO_2. At the start of the experiment, cells were incubated with
531 the indicated drug or DMSO at 37°C for one hour. Following this, cells were incubated
532 for one hr at 37°C with VSV, VSV-MeGFP-V296H, VSV-MeGFP-RABV, VSV-MeGFP-
533 LASV, VSV-MeGFP-LCVM or VSV-MeGFP-ZEBOV in drug or DMSO-containing
534 infection medium (α-MEM, 50mM HEPES, 2% FBS). Cells were then washed to remove
535 non-adsorbed viruses and further incubated at 37°C in medium containing the drug or
536 DMSO with experiments ending at the indicated times by fixation with 3.7%
537 formaldehyde in PBS. Fluorescent intensity from 20,000 single cells from a single round
538 of infection was determined by flow cytometry using a BD FACSCanto™ II equipped
539 with DIVA software package.

540

541 MA104 cells were pretreated for one h with the indicated concentration Apilimod or
542 DMSO. Pretreated cells were inoculated with VSV-eGFP, VSV-eGFP-EBOV or VSV-
543 eGFP-SARS-Cov-2 at an MOI = 1 (based on titers in MA104 cells) in the presence of
544 Apilimod or DMSO for one hour at 37°C. Six to 8 hour post infection, cells were
545 collected and fixed in 2% PFA and then subjected to flow cytometry. The percentage of
546 GFP cells was determined using FlowJo software (Tree Star Industries, Ashland, OR).

547

548 Vero E6 cell monolayers were pretreated for 1 h at 37°C with serial dilutions of Apilimod
549 at the indicated concentrations. Next, SARS-CoV-2 was diluted to an MOI of 0.01 focus-
550 forming units (FFU)/cell in Apilimod-containing medium and added to Vero E6 cells for 1
551 h at 37°C. After adsorption, cells were washed once with PBS, and medium containing
552 the respective concentration of Apilimod was added. Cell were incubated for a 24 h at
553 37°C, and at which time cell culture supernatants were removed and used for
554 determination of viral titer by focus forming assay.

555

556 **SARS-CoV-2 focus forming assay**

557 Cell culture supernatants from virus-infected cells were diluted serially 10-fold and
558 added to Vero E6 cell monolayers in 96-well plates and incubated at 37°C for 1 h.
559 Subsequently, cells were overlaid with 1% (w/v) methylcellulose in MEM supplemented
560 with 2% FBS. Plates were harvested 30 h later by removing overlays and fixed with 4%
561 paraformaldehdye in PBS for 20 min at room temperature. Plates were washed and
562 sequentially incubated with 1 µg/mL of CR3022 anti-spike antibody (51) and HRP-
563 conjugated goat anti-human IgG in PBS supplemented with 0.1% saponin and 0.1%

564 BSA. SARS-CoV-2-infected cell foci were visualized using TrueBlue peroxidase
565 substrate (KPL) and quantitated on an ImmunoSpot microanalyzer (Cellular
566 Technologies). Data were processed using Prism software (GraphPad Prism 8.0) and
567 viral titers are reported as percent inhibition relative to mock-treated SARS-CoV-2
568 infected cells.
569
570 **Entry assay and intracellular traffic**
571 SVG-A cells plated on glass #1.5 coverslips at about 30-40 % confluency one day prior
572 to experiment were treated with drug or DMSO for one hr at 37°C. Following this, cells
573 were incubated at 37°C with VSV, VSV-MeGFP-V296H, VSV-MeGFP-RABV, VSV-
574 MeGFP-LASV, VSV-MeGFP-LCVM or VSV-EBOV (also expressing MeGFP) in drug or
575 DMSO containing infection medium. After this, cells were washed then further incubated
576 in medium containing the drug or DMSO at 37°C with the experiment ending at the
577 indicated time by fixation for 20 min at room temperature with 3.7% formaldehyde in
578 PBS. This was followed with a10-minute incubation of 5µg/mL of Alexa647-labeled
579 wheat germ agglutinin in PBS to label the outline of the cells.
580
581 Cells were imaged using a spinning disk confocal microscope with optical planes
582 spaced 0.3 µm apart (52). The entry assay scored the presence of MeGFP at the
583 nuclear margin in each cell. Trafficking of viruses to endosomal compartments was
584 observed using live-cell imaging using the spinning disc confocal microscope. Time
585 series with images taken every three seconds for two minutes in a single optical plane
586 with the appropriate fluorescent channels (52) were acquired from non-fixed samples
587 imaged at the end of the experimental period. For experiments containing NPC1-Halo,
588 the Halo-tagged cells were labeled with either 250 nM JF549 or JF647 dye in media for
589 30 minutes at 37°C. Following labeling, cells were washed three times with media. The
590 microscope was operated using the Slidebook 6.4 software package (3I) and images
591 were displayed also using this software.
592
593 **Statistical tests**
594 To compare the means from cells with different treatments, one-way ANOVA and the
595 *post-hoc* Tukey test analysis were used to take into account unequal sample sizes as
596 indicated in figure legends.
597

ACKNOWLEDGEMENTS

We thank Walter J. Atwood for providing the parental SVG-A cells, Eric Marino, Justin H. Houser and Tegy John Vadakkan for maintaining the spinning disc confocal microscope (T.K. Lab), Marina Cella and Erica Lantelme from the flow cytometry facility, Department of Pathology and Immunology, WUSM for help with flow cytometry, Stephen C. Harrison for helpful discussions and editorial assistance and Alex J. B. Kreutzberger for editorial help. This research was supported by National Institutes of Health funding (AI109740) to S.P.W. and T.K, by MIRA NIH award (GM130386) to T.K., by National Institutes of Health funding (AI059371) and unrestricted funds from WUSM to S.P.W. and by (75N93019C00062 and R01 AI127828) to M.S.D.

AUTHOR CONTRIBUTIONS (NAMES GIVEN AS INITIALS)

T.K., S.P.W., and M.S.D. were responsible for the overall design of the study; Y.K. carried out virus infection, entry and imaging experiments and prepared figures in the lab of T.K. (Fig. 1-5). P.W.R. designed, generated and characterized VSV-eGFP-SARS-CoV-2 and P.Z.L. carried out VSV-chimera infection experiments in the lab of S.P.W. (Fig. 6). J.B.C. and R.E.C. carried out the experiments with authentic SARS-CoV-2 under BSL3 conditions in the lab of M.S.D. (Fig. 7). Recombinant viruses were generated and characterized by D.K.C., S.P., M.R and T.S. in the lab of S.P.W; T.K. drafted the manuscript and editorially reviewed it in close association with SP.W. and M.S.D; the authors commented on the manuscript.

COMPETING FINANCIAL INTEREST STATEMENT

M.S.D. is a consultant for Inbios, Vir Biotechnology, NGM Biopharmaceuticals, and on the Scientific Advisory Board of Moderna. The Diamond laboratory at Washington University School of Medicine has received sponsored research agreements from Moderna and Emergent BioSolutions.

625 ## REFERENCES

626 1. Chandran K, Sullivan NJ, Felbor U, Whelan SP, Cunningham JM (2005)
627 Endosomal proteolysis of the Ebola virus glycoprotein is necessary for infection.
628 308(5728):1643–1645.

629 2. Carette JE, et al. (2011) Ebola virus entry requires the cholesterol transporter
630 Niemann-Pick C1. *Nature* 477(7364):340–343.

631 3. Huang I-C, et al. (2006) SARS coronavirus, but not human coronavirus NL63,
632 utilizes cathepsin L to infect ACE2-expressing cells. *J Biol Chem* 281(6):3198–
633 3203.

634 4. Simmons G, et al. (2005) Inhibitors of cathepsin L prevent severe acute
635 respiratory syndrome coronavirus entry. *Proc Natl Acad Sci USA* 102(33):11876–
636 11881.

637 5. Ou X, et al. (2020) Characterization of spike glycoprotein of SARS-CoV-2 on virus
638 entry and its immune cross-reactivity with SARS-CoV. *Nat Commun* 11(1):1–12.

639 6. Cao W, et al. (1998) Identification of alpha-dystroglycan as a receptor for
640 lymphocytic choriomeningitis virus and Lassa fever virus. *Science*
641 282(5396):2079–2081.

642 7. Jae LT, et al. (2014) Virus entry. Lassa virus entry requires a trigger-induced
643 receptor switch. *Science* 344(6191):1506–1510.

644 8. Pasqual G, Rojek JM, Masin M, Chatton J-Y, Kunz S (2011) Old world
645 arenaviruses enter the host cell via the multivesicular body and depend on the
646 endosomal sorting complex required for transport. *PLoS Pathog* 7(9):e1002232.

647 9. Carlton JG, Cullen PJ (2005) Coincidence detection in phosphoinositide signaling.
648 *Trends Cell Biol* 15(10):540–547.

649 10. Sbrissa D, Ikonomov OC, Shisheva A (1999) PIKfyve, a mammalian ortholog of
650 yeast Fab1p lipid kinase, synthesizes 5-phosphoinositides. Effect of insulin. *J Biol*
651 *Chem* 274(31):21589–21597.

652 11. Shisheva A, Sbrissa D, Ikonomov O (1999) Cloning, characterization, and

653 expression of a novel Zn2+-binding FYVE finger-containing phosphoinositide
654 kinase in insulin-sensitive cells. *Mol Cell Biol* 19(1):623–634.

655 12. Ikonomov OC, Sbrissa D, Shisheva A (2001) Mammalian cell morphology and
656 endocytic membrane homeostasis require enzymatically active phosphoinositide
657 5-kinase PIKfyve. *J Biol Chem* 276(28):26141–26147.

658 13. Rutherford AC, et al. (2006) The mammalian phosphatidylinositol 3-phosphate 5-
659 kinase (PIKfyve) regulates endosome-to-TGN retrograde transport. *J Cell Sci*
660 119(Pt 19):3944–3957.

661 14. Sbrissa D, et al. (2007) Core protein machinery for mammalian
662 phosphatidylinositol 3,5-bisphosphate synthesis and turnover that regulates the
663 progression of endosomal transport. Novel Sac phosphatase joins the ArPIKfyve-
664 PIKfyve complex. *J Biol Chem* 282(33):23878–23891.

665 15. Ikonomov OC, et al. (2002) Functional dissection of lipid and protein kinase
666 signals of PIKfyve reveals the role of PtdIns 3,5-P2 production for endomembrane
667 integrity. *J Biol Chem* 277(11):9206–9211.

668 16. Jefferies HBJ, et al. (2008) A selective PIKfyve inhibitor blocks PtdIns(3,5)P(2)
669 production and disrupts endomembrane transport and retroviral budding. *EMBO*
670 *Rep* 9(2):164–170.

671 17. Sano O, et al. (2016) Vacuolin-1 inhibits autophagy by impairing lysosomal
672 maturation via PIKfyve inhibition. *FEBS Lett* 590(11):1576–1585.

673 18. Cerny J, et al. (2004) The small chemical vacuolin-1 inhibits Ca(2+)-dependent
674 lysosomal exocytosis but not cell resealing. *EMBO Rep* 5(9):883–888.

675 19. Cai X, et al. (2013) PIKfyve, a class III PI kinase, is the target of the small
676 molecular IL-12/IL-23 inhibitor apilimod and a player in Toll-like receptor signaling.
677 *Chem Biol* 20(7):912–921.

678 20. Sharma G, et al. (2019) A family of PIKFYVE inhibitors with therapeutic potential
679 against autophagy-dependent cancer cells disrupt multiple events in lysosome
680 homeostasis. *Autophagy* 15(10):1694–1718.

681 21. Ikonomov OC, et al. (2003) Active PIKfyve associates with and promotes the

682 membrane attachment of the late endosome-to-trans-Golgi network transport
683 factor Rab9 effector p40. *J Biol Chem* 278(51):50863–50871.

684 22. Chen C, et al. (2017) Identification of Novel Vacuolin-1 Analogues as Autophagy
685 Inhibitors by Virtual Drug Screening and Chemical Synthesis. *Molecules*
686 22(6):891.

687 23. Lu Y, et al. (2014) Vacuolin-1 potently and reversibly inhibits autophagosome-
688 lysosome fusion by activating RAB5A. *Autophagy* 10(11):1895–1905.

689 24. Sands BE, et al. (2010) Randomized, double-blind, placebo-controlled trial of the
690 oral interleukin-12/23 inhibitor apilimod mesylate for treatment of active Crohn's
691 disease. *Inflamm Bowel Dis* 16(7):1209–1218.

692 25. Wada Y, et al. (2012) Apilimod inhibits the production of IL-12 and IL-23 and
693 reduces dendritic cell infiltration in psoriasis. *PLoS ONE* 7(4):e35069.

694 26. Nelson EA, et al. (2017) The phosphatidylinositol-3-phosphate 5-kinase inhibitor
695 apilimod blocks filoviral entry and infection. *PLoS Negl Trop Dis* 11(4):e0005540.

696 27. Qiu S, et al. (2018) Ebola virus requires phosphatidylinositol (3,5) bisphosphate
697 production for efficient viral entry. *Virology* 513:17–28.

698 28. Spence JS, Krause TB, Mittler E, Jangra RK, Chandran K (2016) Direct
699 Visualization of Ebola Virus Fusion Triggering in the Endocytic Pathway. *MBio*
700 7(1):e01857–15.

701 29. Burakoff R, et al. (2006) A phase 1/2A trial of STA 5326, an oral interleukin-12/23
702 inhibitor, in patients with active moderate to severe Crohn's disease. *Inflamm*
703 *Bowel Dis* 12(7):558–565.

704 30. Krausz S, et al. (2012) Brief report: a phase IIa, randomized, double-blind,
705 placebo-controlled trial of apilimod mesylate, an interleukin-12/interleukin-23
706 inhibitor, in patients with rheumatoid arthritis. *Arthritis Rheum* 64(6):1750–1755.

707 31. Hulseberg CE, et al. (2019) Arbidol and Other Low-Molecular-Weight Drugs That
708 Inhibit Lassa and Ebola Viruses. *J Virol* 93(8):11.

709 32. Dyall J, et al. (2018) Identification of Combinations of Approved Drugs With

710 Synergistic Activity Against Ebola Virus in Cell Cultures. *J Infect Dis*
711 218(suppl_5):S672–S678.

712 33. Bago R, et al. (2014) Characterization of VPS34-IN1, a selective inhibitor of
713 Vps34, reveals that the phosphatidylinositol 3-phosphate-binding SGK3 protein
714 kinase is a downstream target of class III phosphoinositide 3-kinase. *Biochem J*
715 463(3):413–427.

716 34. Glowacka I, et al. (2011) Evidence that TMPRSS2 activates the severe acute
717 respiratory syndrome coronavirus spike protein for membrane fusion and reduces
718 viral control by the humoral immune response. *J Virol* 85(9):4122–4134.

719 35. Shulla A, et al. (2011) A transmembrane serine protease is linked to the severe
720 acute respiratory syndrome coronavirus receptor and activates virus entry. *J Virol*
721 85(2):873–882.

722 36. Matsuyama S, et al. (2010) Efficient activation of the severe acute respiratory
723 syndrome coronavirus spike protein by the transmembrane protease TMPRSS2. *J*
724 *Virol* 84(24):12658–12664.

725 37. Hoffmann M, et al. (2020) SARS-CoV-2 Cell Entry Depends on ACE2 and
726 TMPRSS2 and Is Blocked by a Clinically Proven Protease Inhibitor. *Cell*
727 181(2):271–280.e8.

728 38. Simmons G, et al. (2004) Characterization of severe acute respiratory syndrome-
729 associated coronavirus (SARS-CoV) spike glycoprotein-mediated viral entry. *Proc*
730 *Natl Acad Sci USA* 101(12):4240–4245.

731 39. Gayle S, et al. (2017) Identification of apilimod as a first-in-class PIKfyve kinase
732 inhibitor for treatment of B-cell non-Hodgkin lymphoma. *Blood* 129(13):1768–
733 1778.

734 40. Nelson CDS, Derdowski A, Maginnis MS, O'Hara BA, Atwood WJ (2012) The VP1
735 subunit of JC polyomavirus recapitulates early events in viral trafficking and is a
736 novel tool to study polyomavirus entry. *Virology* 428(1):30–40.

737 41. Baranov MV, et al. (2019) The Phosphoinositide Kinase PIKfyve Promotes
738 Cathepsin-S-Mediated Major Histocompatibility Complex Class II Antigen
739 Presentation. *iScience* 11:160–177.

740 42. Côté M, et al. (2011) Small molecule inhibitors reveal Niemann-Pick C1 is
741 essential for Ebola virus infection. *Nature* 477(7364):344–348.

742 43. Le Blanc I, et al. (2005) Endosome-to-cytosol transport of viral nucleocapsids. *Nat*
743 *Cell Biol* 7(7):653–664.

744 44. Zhou Y, et al. (2015) Protease inhibitors targeting coronavirus and filovirus entry.
745 *Antiviral Res* 116:76–84.

746 45. Soh TK, Whelan SPJ (2015) Tracking the Fate of Genetically Distinct Vesicular
747 Stomatitis Virus Matrix Proteins Highlights the Role for Late Domains in
748 Assembly. 89(23):11750–11760.

749 46. Piccinotti S, Kirchhausen T, Whelan SPJ (2013) Uptake of rabies virus into
750 epithelial cells by clathrin-mediated endocytosis depends upon actin.
751 87(21):11637–11647.

752 47. Wong AC, Sandesara RG, Mulherkar N, Whelan SP, Chandran K (2010) A
753 forward genetic strategy reveals destabilizing mutations in the Ebolavirus
754 glycoprotein that alter its protease dependence during cell entry. *J Virol*
755 84(1):163–175.

756 48. Whelan SP, Ball LA, Barr JN, Wertz GT (1995) Efficient recovery of infectious
757 vesicular stomatitis virus entirely from cDNA clones. *Proc Natl Acad Sci USA*
758 92(18):8388–8392.

759 49. Ran FA, et al. (2013) Genome engineering using the CRISPR-Cas9 system. *Nat*
760 *Protoc* 8(11):2281–2308.

761 50. Chou Y-Y, et al. (2016) Identification and characterization of a novel broad
762 spectrum virus entry inhibitor. 90(9):4494–4510.

763 51. Yuan M, et al. (2020) A highly conserved cryptic epitope in the receptor-binding
764 domains of SARS-CoV-2 and SARS-CoV. *Science*:eabb7269.

765 52. Cocucci E, Aguet F, Boulant S, Kirchhausen T (2012) The first five seconds in the
766 life of a clathrin-coated pit. 150(3):495–507.

767

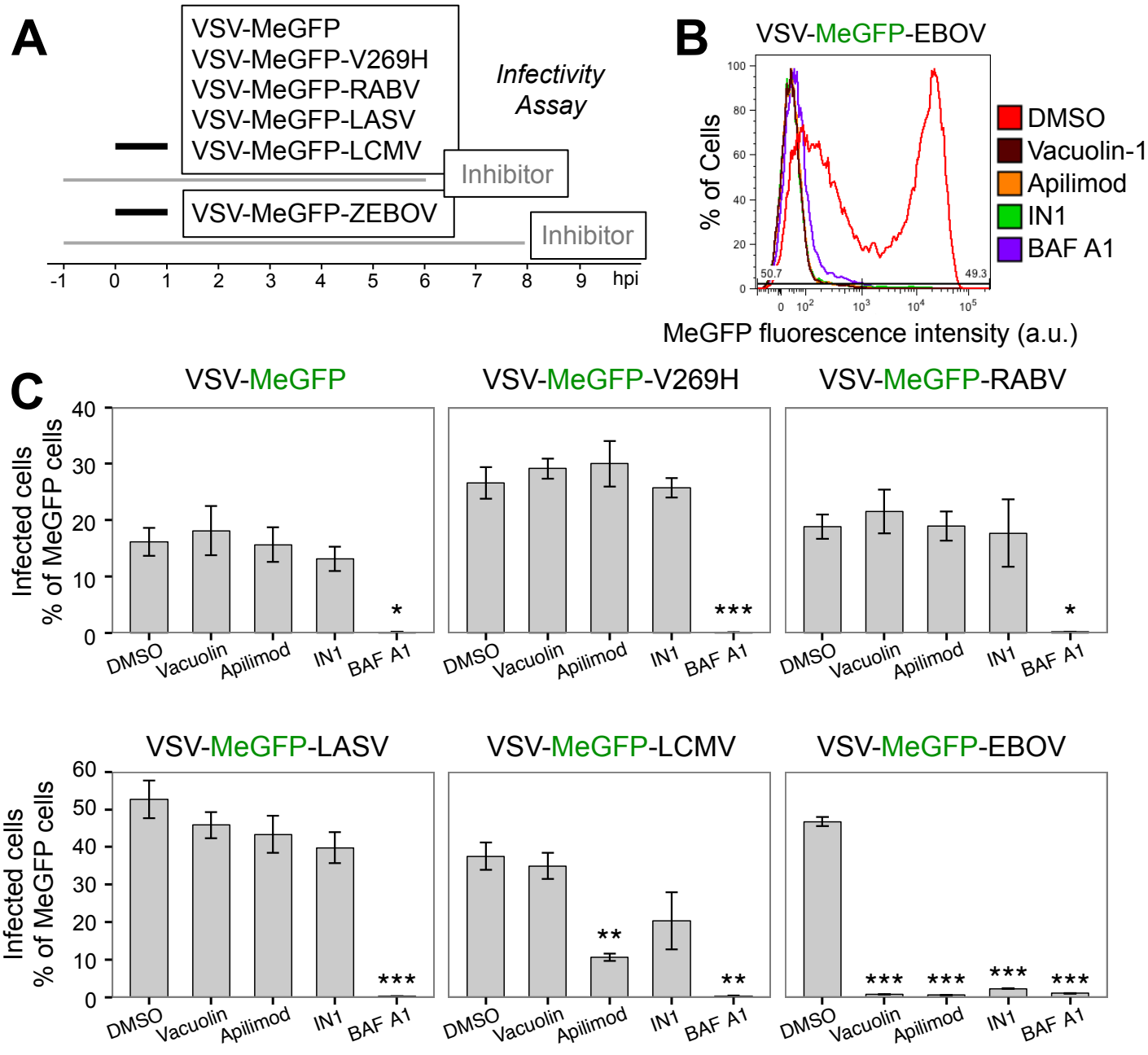
A
VSV-MeGFP
VSV-MeGFP-V269H
VSV-MeGFP-RABV
VSV-MeGFP-LASV
VSV-MeGFP-LCMV
Infectivity Assay
Inhibitor
VSV-MeGFP-ZEBOV
Inhibitor
-1 0 1 2 3 4 5 6 7 8 9 hpi
B
VSV-MeGFP-EBOV
% of Cells
50.7
49.3
MeGFP fluorescence intensity (a.u.)
DMSO
Vacuolin-1
Apilimod
IN1
BAF A1
C
VSV-MeGFP
VSV-MeGFP-V269H
VSV-MeGFP-RABV
VSV-MeGFP-LASV
VSV-MeGFP-LCMV
VSV-MeGFP-EBOV
Infected cells
% of MeGFP cells
DMSO
Vacuolin
Apilimod
IN1
BAF A1

Figure 1

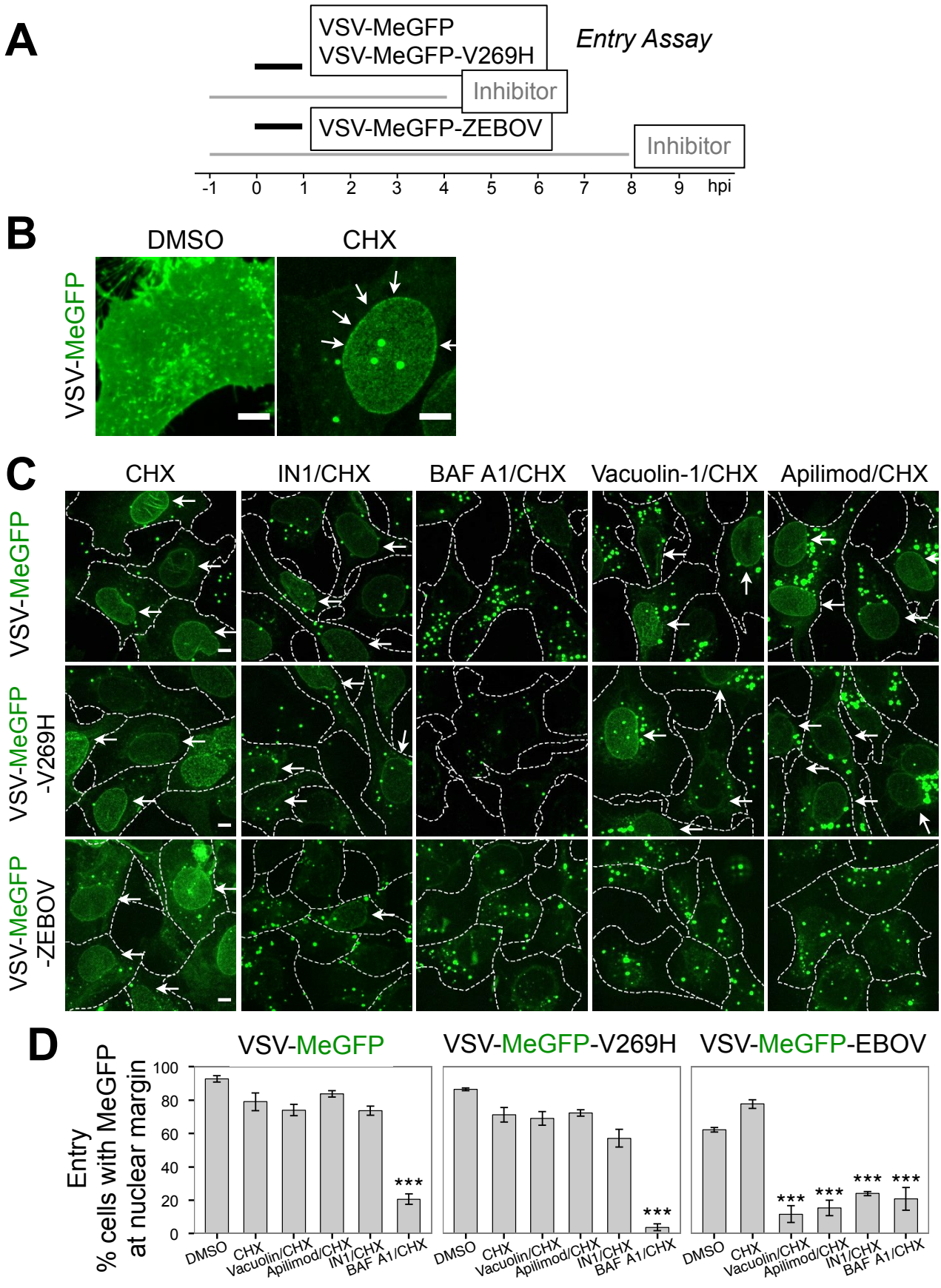
A
VSV-MeGFP
VSV-MeGFP-V269H
Entry Assay
Inhibitor
VSV-MeGFP-ZEBOV
Inhibitor
-1 0 1 2 3 4 5 6 7 8 9 hpi
B
DMSO
CHX
VSV-MeGFP
C
CHX
IN1/CHX
BAF A1/CHX
Vacuolin-1/CHX
Apilimod/CHX
VSV-MeGFP
VSV-MeGFP -V269H
VSV-MeGFP -ZEBOV
D
VSV-MeGFP
VSV-MeGFP-V269H
VSV-MeGFP-EBOV
Entry
% cells with MeGFP at nuclear margin
100
80
60
40
20
0
***
DMSO
CHX
Vacuolin/CHX
Apilimod/CHX
IN1/CHX
BAF A1/CHX

Figure 2

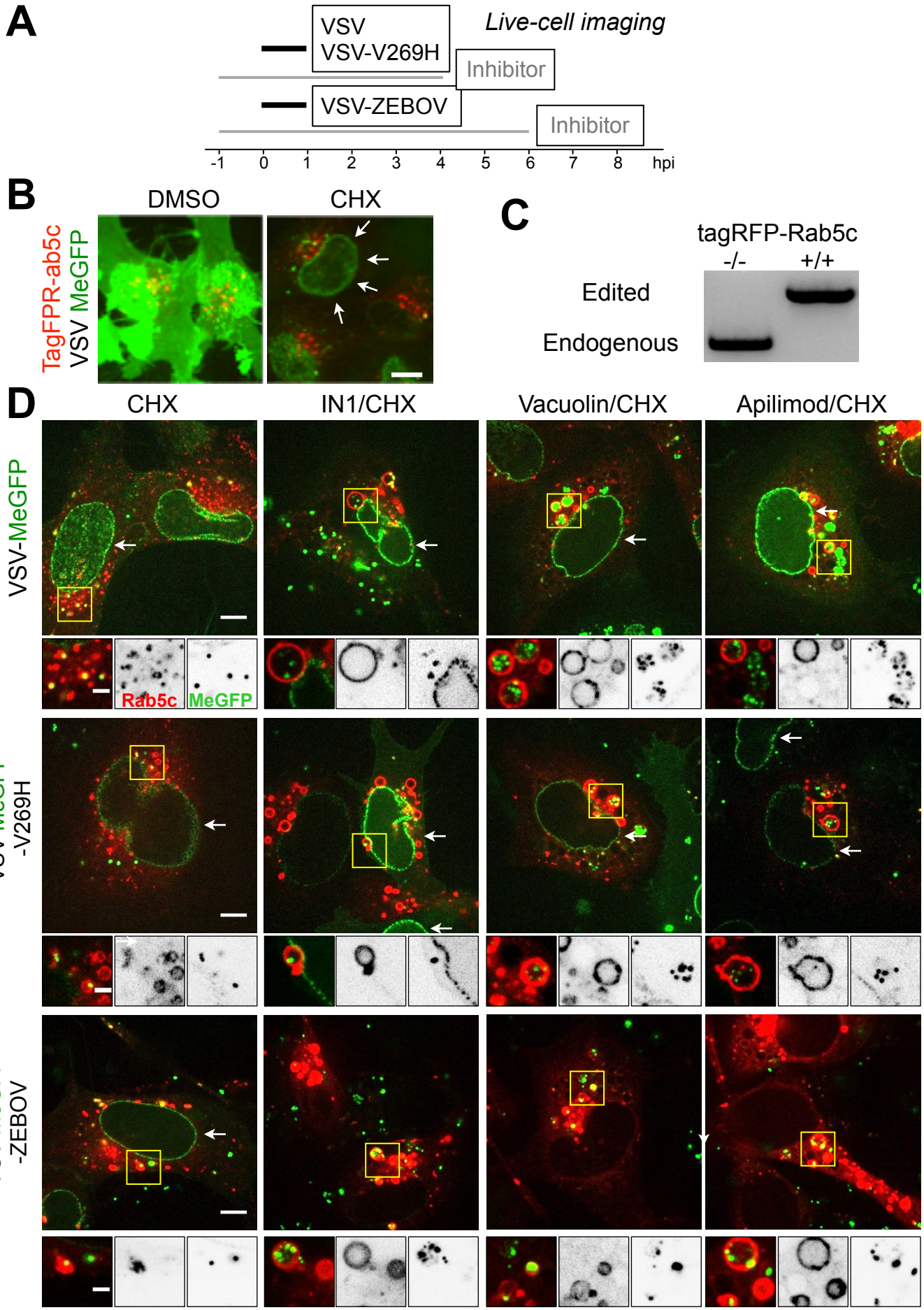
A
VSV
VSV-V269H
Live-cell imaging
Inhibitor
VSV-ZEBOV
Inhibitor
-1
0
1
2
3
4
5
6
7
8
hpi
B
DMSO
CHX
TagFPR-ab5c
VSV MeGFP
C
tagRFP-Rab5c
-/-
+/+
Edited
Endogenous
D
CHX
IN1/CHX
Vacuolin/CHX
Apilimod/CHX
VSV-MeGFP
Rab5c
MeGFP
VSV-MeGFP
-V269H
VSV-MeGFP
-ZEBOV

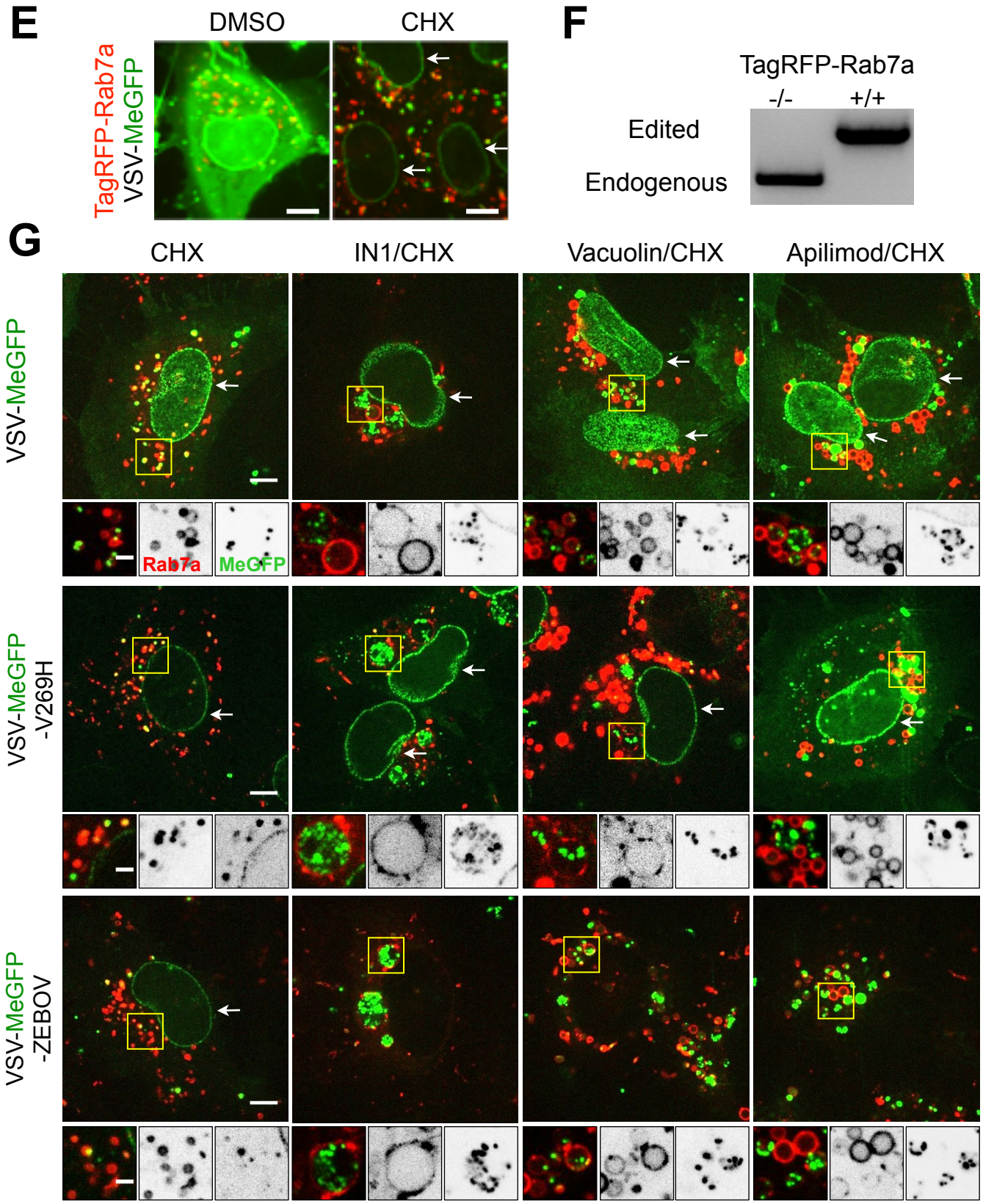
E
DMSO
CHX
TagRFP-Rab7a
VSV-MeGFP
F
TagRFP-Rab7a
-/-
+/+
Edited
Endogenous
G
CHX
IN1/CHX
Vacuolin/CHX
Apilimod/CHX
VSV-MeGFP
Rab7a
MeGFP
VSV-MeGFP
-V269H
VSV-MeGFP
-ZEBOV

Figure 3

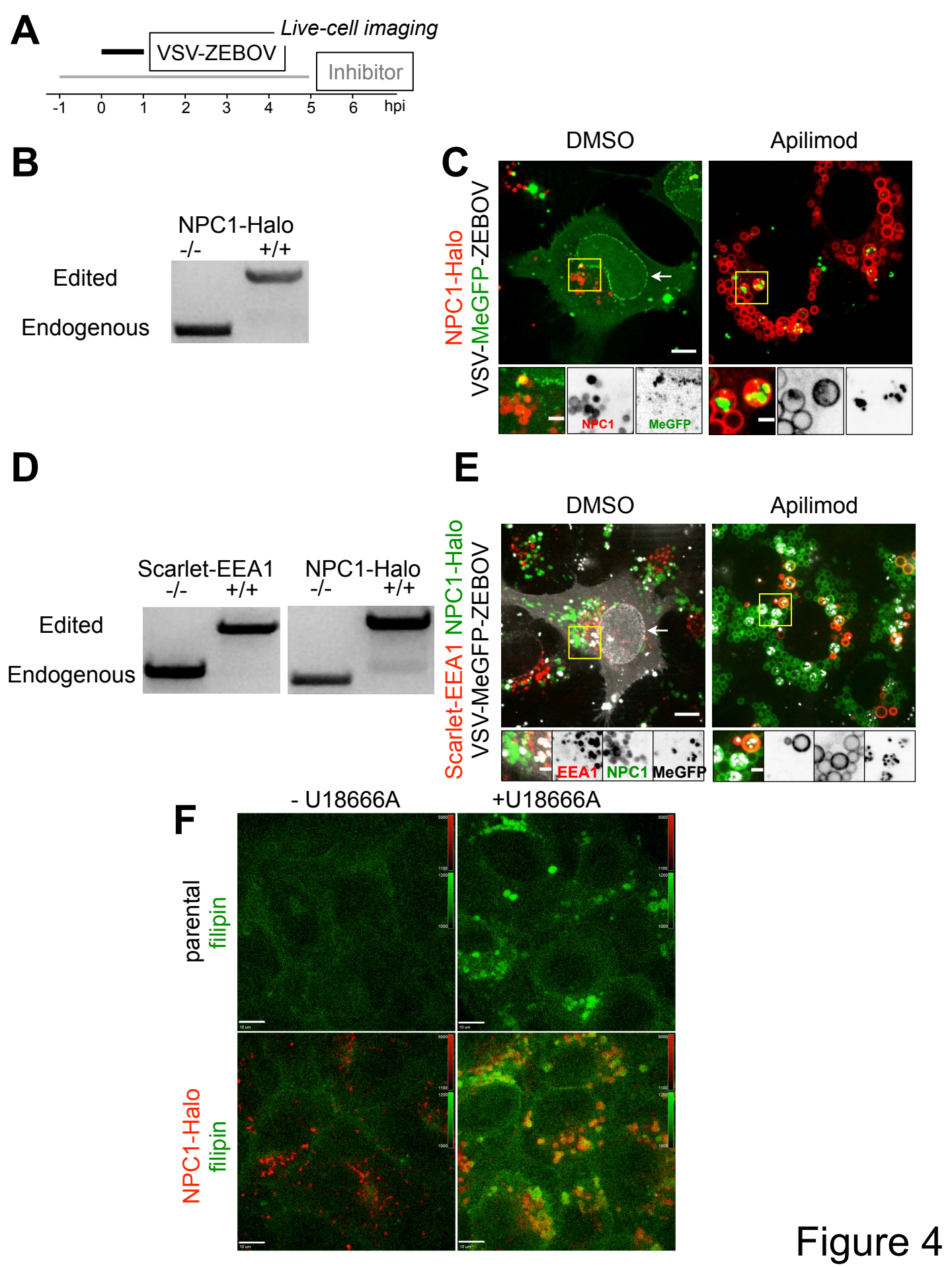
A
Live-cell imaging
VSV-ZEBOV
Inhibitor
-1
0
1
2
3
4
5
6
hpi
B
NPC1-Halo
-/-
+/+
Edited
Endogenous
C
DMSO
Apilimod
NPC1-Halo
VSV-MeGFP-ZEBOV
NPC1
MeGFP
D
Scarlet-EEA1
NPC1-Halo
-/-
+/+
-/-
+/+
Edited
Endogenous
E
DMSO
Apilimod
Scarlet-EEA1 NPC1-Halo
VSV-MeGFP-ZEBOV
EEA1
NPC1
MeGFP
F
- U18666A
+U18666A
parental
filipin
NPC1-Halo
filipin

Figure 4

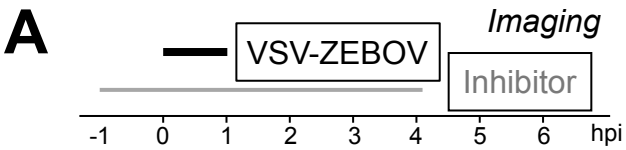

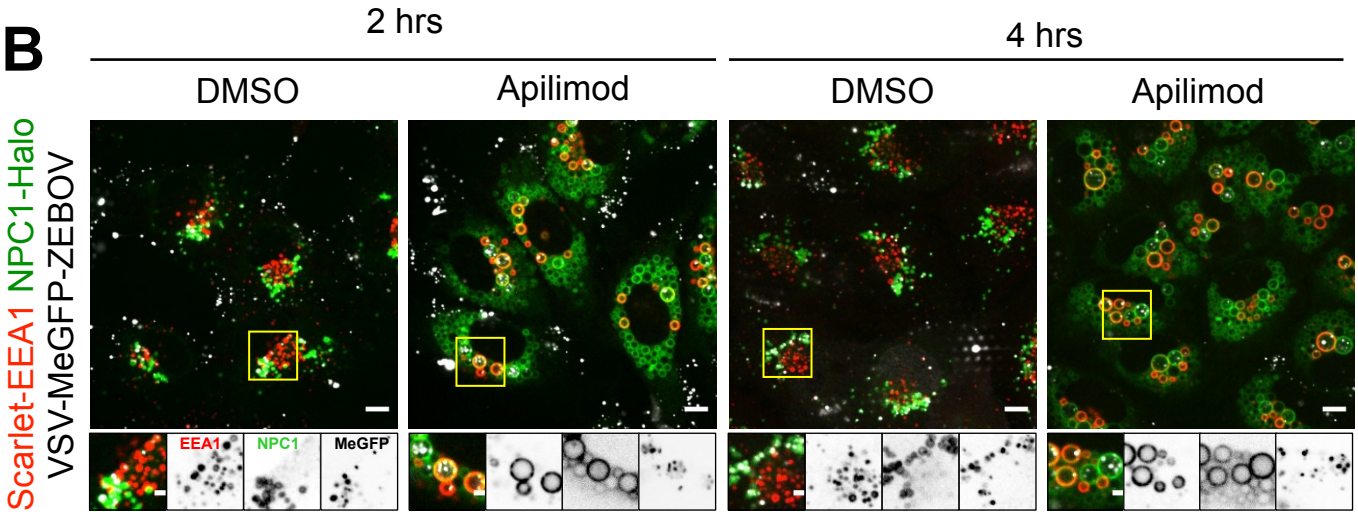

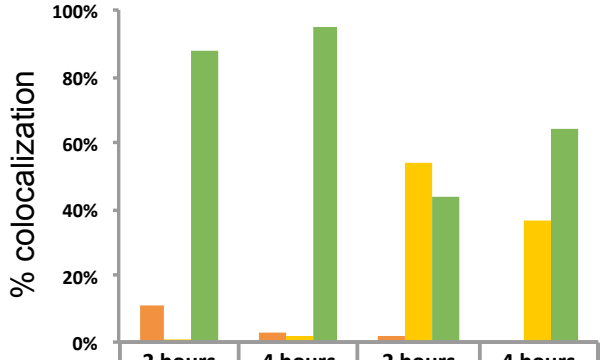

	DMSO 2 hours	DMSO 4 hours	Apilimod 2 hours	Apilimod 4 hours
EEA1/Total	11%	3%	2%	0%
EEA1 NPC1/Total	0%	2%	54%	36%
NPC1/Total	88%	95%	44%	64%

Figure 5

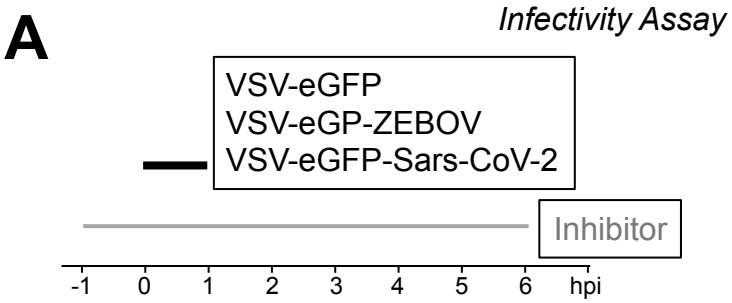
A
Infectivity Assay
VSV-eGFP
VSV-eGP-ZEBOV
VSV-eGFP-Sars-CoV-2
Inhibitor
-1
0
1
2
3
4
5
6
hpi

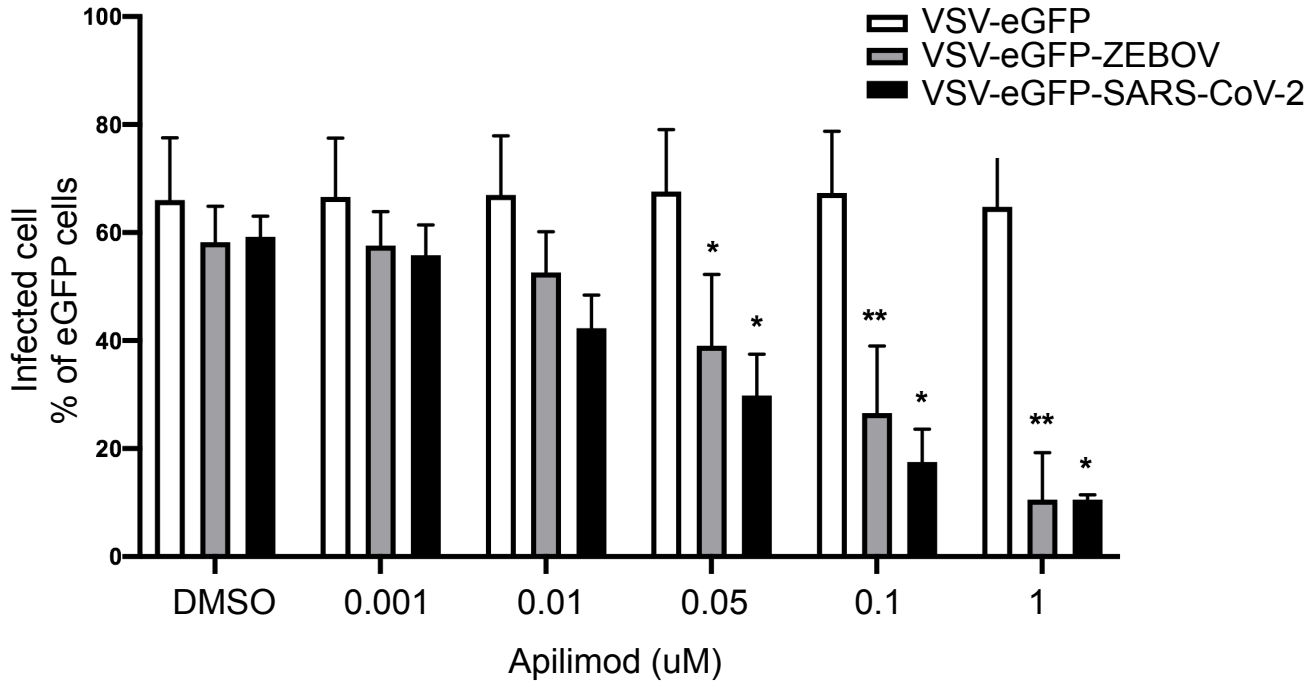
B
VSV-eGFP
VSV-eGFP-ZEBOV
VSV-eGFP-SARS-CoV-2
Infected cell
% of eGFP cells
100
80
60
40
20
0
*
*
**
*
**
*
DMSO
0.001
0.01
0.05
0.1
1
Apilimod (uM)

Figure 6

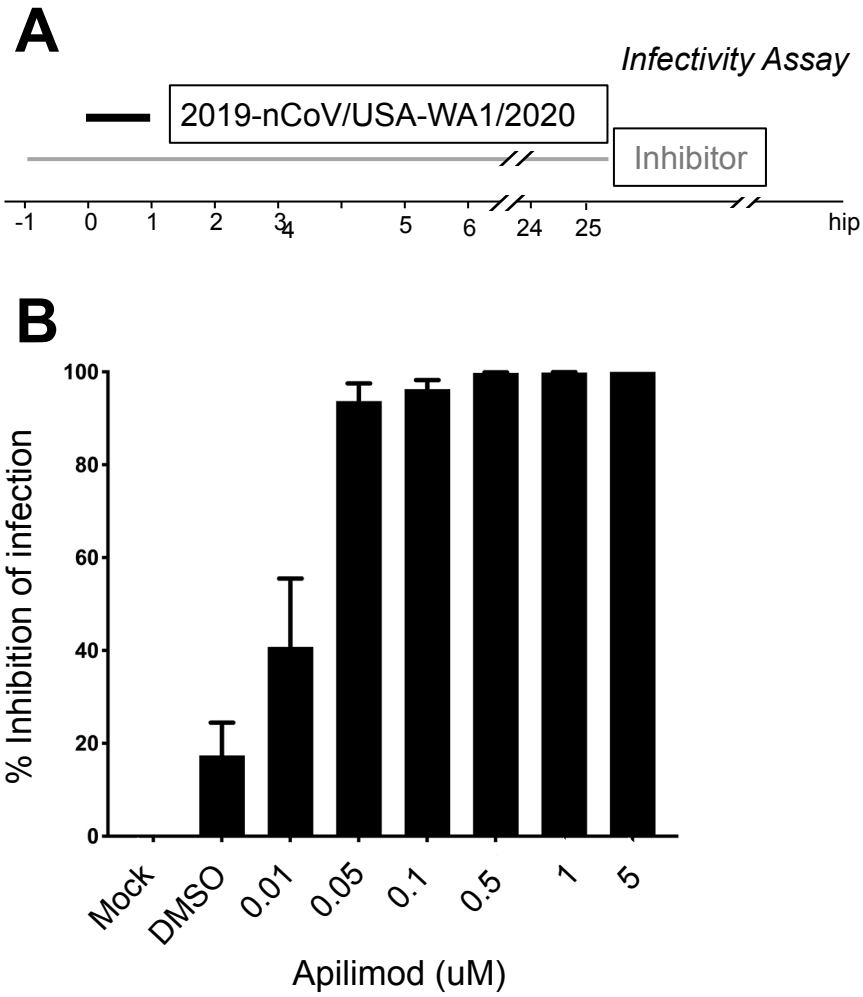
A
Infectivity Assay
2019-nCoV/USA-WA1/2020
Inhibitor
-1
0
1
2
3
4
5
6
24
25
hip
B
% Inhibition of infection
100
80
60
40
20
0
Mock
DMSO
0.01
0.05
0.1
0.5
1
5
Apilimod (uM)

Figure 7